The performance of ES-FEM with automatic triangle mesh adaptation in engineering mechanics applications

***Le Hoang Vu, †Sawekchai Tangaramvong,**

Applied Mechanics and Structures Research Unit
Department of Civil Engineering, Chulalongkorn University, Thailand.

*Presenting author: lehoangvu.chula.11793@gmail.com
†Corresponding author: sawekchai.t@chula.ac.th

Abstract

This paper theoretical studies the performance of automatic adaptive edge-based smoothed finite element method (ES-FEM) for the solutions of elastic in-plane engineering mechanics problems. An ES-FEM adopting a strain smoothing technique over the edges of a generic triangular mesh presents coarse mesh accuracy in numerical analysis results. The automatic refinement of model construction from coarse-to-fine of meshes associated with high intensity of stresses and vice versa for others with low stress intensity. The specific L2-norm error, in a similar fashion to Zienkiewicz–Zhu, estimator indicates the difference between numerical von Mises stress solutions and recovery stresses underpinning the structural model with applied forces. A number of benchmarks, i.e. especially those subjected to stress singularity and/or incompressibility conditions, have been adopted for the comparisons in views of solution accuracy and computational robustness between ES-FEM and some standard isoparametric finite element model. Significant improvement in the computing efficiency and hence solution convergence has been clearly evidenced as when the ES-FEM analysis was encoded with the automatic model adaptation and vectorization within MATLAB environment, simultaneously.

Keywords: ES-FEM, Automatic Adaptive Mesh, Posterior Error Estimator, Vectorization.

Introduction

Smoothed finite element methods (S-FEMs) have been successfully applied in solving many engineering mechanics problems. [1] combined the finite element method (FEM) to some of the meshfree techniques. Besides the information at nodes on each element S-FEM models consider nodal unknowns of neighboring elements to construct smoothed strain field to enhance stability, convergence and accuracy of the solutions. The diversity of two-dimensional S-FEMs which are edge-, nodal- and cell-based S-FEMs with different properties is created by applying the strain smoothing technique from [2]. With the smoothed strain field, these models exhibit desirable properties and work well with a general n-side polygonal elements, especially for the three-node triangular (T3) meshes. Among the above S-FEM models, the Edge-based Smoothed Finite Element Method (ES-FEM) have arisen as the most outstanding S-FEM model which possesses so many advantages such as stable both spatially and temporally, much more accurate compared with many available FEMs. The ES-FEM creates models with close-to-exact stiffness so that it is efficient for solving both static and dynamic problems.

For mechanics problems associated with physically instabilizing stress singularity, the standard model construction has experienced the low accuracy of results using standard finite elements. A process of iterative mesh reconstruction will automatically decide where high

density of mesh are required to obtain a proper mesh distribution in each step of analysis. A layer of singular five-node elements will be applied around the crack-tip to capture the theoretical occurrence of unbounded stresses. Modifications in error assessment procedure for these elements are presented to accurately converge the stress response results over the local areas of structures considered.

The method [3] employed standard Delaunay triangulation procedure without any error indicator, considered as a geometric dependent refinement. In addition, a singular ES-FEM [4] adopted a recovery-based error indicator in an energy norm to predict accurately singular stress field around re-entrant corners. The applications of the node-based smoothed finite element method (NS-FEM) using the similar recovery-based error function were described in [5]. where it demonstrated clearly the good convergence capability and upper-bound strain energy solutions over iterative mesh reconstruction processes.

However, it is uncommon that the researchers interested in adaptive analysis showed the results in terms of runtime or computing resources in the past. The ES-FEM-T3 models incorporating a simple yet effective recovery-based error function of von Mises stresses were encoded within a vector-oriented MATLAB environment. The newest node bisection algorithm was adopted to the automatic AMR procedures. In essence, a parent triangle element is sub-divided into several children triangle elements along the longest edge to eliminate hanging nodes. The effciency of the present models is tested by using the two problems, from which successfully solved by [6]-[7], in providing solutions of such challenging problems under the presence of stress singularity and discontinuity field. Moreover, the proposed analysis framework also describes a significant reduction of computing resources as compared to an uniform model construction strategy.

The following section includes a brief description of ES-FEM-T3 formulations and displacement interpolation within a singular element. Then, an overview of the recovery-based stress adaptive mesh algorithm incorporated with the longest-edge refinement technique is provided. In the next Section, two numerical examples subjected to the challenging of elastic stress singularity and discontinuity are given to illustrate applications of the developed analysis scheme. They also highlight the accuracy and robustness of the proposed ES-FEM-T3 framework. The main conclusion and suggestion for future research are drawn in the end part.

Brief description of the ES-FEM model

An Overview of The ES-FEM Using Triangular Elements

A set of $N_s = N_{eg}$ for both ”non-overlap” and “no-gap” smoothing domains Ω_k^s will fill in the whole problem domain $\Omega = \cup_{k=1}^{N_s} \Omega_k^s$ and $\Omega_i^s \cap \Omega_j^s = \varnothing,\ i \neq j$. The strains of generic ES-FEM-T3 elements are smoothed over the smoothing domains by connecting between two endpoints of the edge and central points of neighboring elements.
The smoothing strain operator over the edge-based smoothing domain Ω_k^s can be defined by:

$$\bar{\varepsilon}_k = \int_{\Omega_k^s} \tilde{\varepsilon}(x) W(x) d\Omega \tag{1}$$

where $\tilde{\varepsilon}(x)$ is the compatible strain field in FEM-T3, and $W(x)$ is a weight function as

$$W(x)=\begin{cases}1/A_k^s, & x\in\Omega_k^s \\ 0, & x\notin\Omega_k^s\end{cases} \quad \& \int_{\Omega_k^s} W(x)d\Omega=1 \tag{2}$$

A Green's divergence theorem is applied and yields the following smoothed strains:

$$\bar{\varepsilon}_k=\frac{1}{A_k^s}\int_{\Omega_k^s}\tilde{\varepsilon}(x)d\Omega=\int_{\Omega_k^s}L_d\left[\bar{u}(x)\right]W(x)d\Omega=\frac{1}{A_k^s}\int_{\Gamma_k^s}L_n(x)\bar{u}(x)d\Gamma \tag{3}$$

where $L_n(x)$ is a matrix of containing the outward normal vectors to the boundary Γ_k^s as depicted in Fig. 1, $A_k^s=\int_{\Omega_k^s}d\Omega=\frac{1}{3}\sum_{j=1}^{N_e^k}A_j$ is the area of smoothing domain Ω_k^s, N_e^k is the number of elements containing edge k.

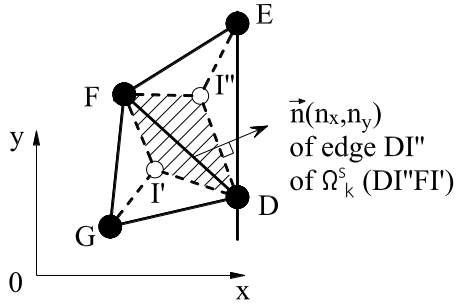

Figure 1. Outward normal to the edge DI'' under the smoothing domain DI''-FI' in x-y coordinates

The smoothed strain–displacement matrix $\bar{B}_i(x,y)$ of node i-th is constructed by having

$$\bar{B}_i=\frac{1}{A_k^s}\int_{\Gamma_k^s}L_n(x)N_i(x)d\Gamma=\begin{bmatrix}\bar{b}_{ix} & 0\\ 0 & \bar{b}_{iy}\\ \bar{b}_{iy} & \bar{b}_{ix}\end{bmatrix} \text{ with } \bar{b}_{ix(y)}=\frac{1}{A_k^s}\int_{\Gamma_k^s}n_{x(y)}(x)N_i(x)d\Gamma \tag{4}$$

One single Gauss's integration point is applied for each q-th segment $\Gamma_{k,q}^s$ of the boundary Γ_k^s

$$\bar{b}_{ix(y)}=\frac{1}{A_k^s}\sum_{p=1}^{n_\Gamma^s}n_{x(y),\mathrm{p}}(x)N_i\left(x_p^{Gauss}\right)\mathrm{l}_p \tag{5}$$

where n_Γ^s is the total number of boundary segments $\Gamma_{k,q}^s\in\Gamma_k^s$, x_p^{Gauss} are the coordinates of a Gauss's point on the boundary segment $\Gamma_{k,q}^s$, $n_{x(y),p}$ and l_p denote the unit normal and the length of the boundary q-th segment $\Gamma_{k,q}^s$.

An ES-FEM Formulation Using A Layer of Singular Elements

Problems with a re-entrant corner as introduced by [8] have the singular stress field of arbitrary order. The power singular term λ, depends only on the vertex angles of $\pi<\phi\le 2\pi$. [9] and [10] theoretically showed the occurrence of elastic stress singularities at angular corners resulting from various BCs rather than only the free-free BC as normally encountered in crack problems. The λ (in the term $\sigma\sim r^{\lambda-1}$) is interpolated from the graph as provided in

[9] or computed from the characteristic equations in [10] depending on the value of vertex angle and the BCs on the two radial edges.

The linear interpolation used in standard finite elements cannot reproduce such a singular field. The most widely used technique to simulate this kind of stress singularity is the so-called (quadratic) 6-node crack-tip element in which the additional midpoint are shifted by a quarter edge-lengths toward the crack-tip. The singularity is then achieved nicely by the well-known iso-parametric mapping procedure [11]. In the present singular ES-FEM-T3 method, however, no mapping is needed and only the shape function values (not the derivatives) are required. Making use of this important feature of ES-FEM-T3, the stress singularity at the crack tip can be created by a simple point interpolation method with extra basis functions of proper fractional order polynomials.

The domain with a horizontal opening crack is discretized using a layer of five-noded triangular elements that contribute to the crack-tip and standard three-node triangular elements in the remaining area as in Fig. 2a). Only an additional node on each edge that directly connected to the singular point is added in general at any point Fig. 2b) that can produce a proper order of stress singularity near the crack tip.

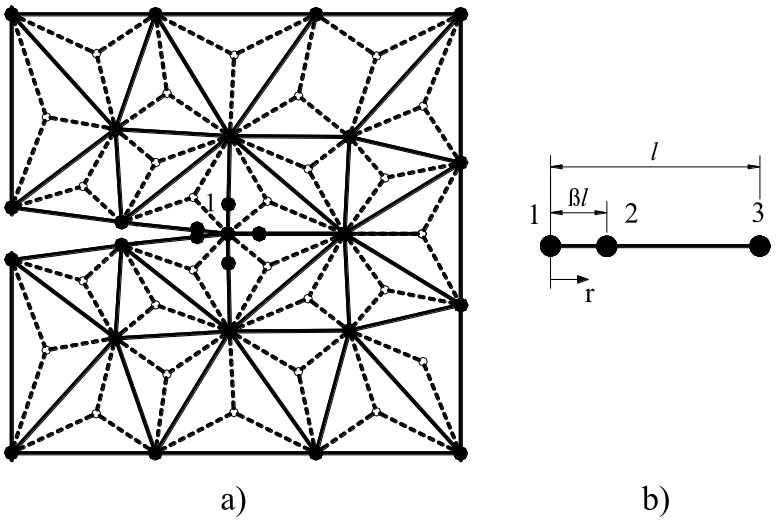

Figure 2. a) Triangular mesh with layer of five-node elements in the ES-FEM-T3,

b) Additional node at arbitrary location in radial coordinate originated at the crack-tip

The displacement field, u, along the crack-tip element edge is approximated using:

$$u(x) = P^T(x)c = c_0 + c_1 r + c_2 r^{\lambda} \tag{6}$$

where $0 \le r \le l$ is the radial coordinate originated at the crack-tip (node 1 in Fig. 2b), and $c_i (i = 0,1,2)$ are the coefficients yet to be determined, $1/2 \le \lambda < 1$ is a singularity parameter.

The unknown coefficients c can be obtained by substituting the radial coordinates of nodes into Eq. (6). Then, we replace it in the same equation to get the matrix form as given follows:

$$u(x) = \begin{bmatrix} \Phi_1 & \Phi_2 & \Phi_3 \end{bmatrix} \begin{Bmatrix} u_1 & u_2 & u_3 \end{Bmatrix}^T = \Phi(x) d \tag{7}$$

where $\Phi_i (i = 1,2,3)$ are shape functions corresponding to the three nodes on the edge that directly connected to the crack-tip and is defined as follows:

$$\Phi_1 = 1 + \frac{r^\lambda(\beta - 1) + l^{\lambda-1}(1-\beta^\lambda)r}{(\beta l)^\lambda - \beta l^\lambda}, \Phi_2 = \frac{r^\lambda - l^{\lambda-1}r}{(\beta l)^\lambda - \beta l^\lambda}, \Phi_3 = \frac{l^{\lambda-1}\beta^\lambda r - \beta r^\lambda}{(\beta l)^\lambda - \beta l^\lambda} \tag{8}$$

and $u_i (i = 1,2,3)$ are the nodal displacements, l is the length of the element edge, and $0 \le \beta \le 1$ is the propotion of the edge 1-2 over the edge 1-3.

For fracture mechanics problems with in-line crack faces, $\lambda = 1/2$, and simply take $\beta = 1/4$, the shape functions become

$$\Phi_1 = 1 + 2\frac{r}{l} - 3\sqrt{\frac{r}{l}},\ \Phi_2 = -4\frac{r}{l} + 4\sqrt{\frac{r}{l}},\ \Phi_3 = 2\frac{r}{l} - \sqrt{\frac{r}{l}} \tag{9}$$

These $\Phi_i (i = 1,2,3)$ satisfy all the basic properties of a shape function such as linear reproducibility, Partition of Unity, Kronecker Delta properties and can actually produce the singularity of stress field with the power of 1/2 near the crack-tip.

In the radial direction, the displacement field takes the enriched form as given in Eq. (6), while in the tangential direction it is assumed to be linearly dependent to ensure the compatibility along the two-node edge of crack-tip elements. Now, we consider the five-node element 1-4-2-3-5 and two layers of singular smoothing domains are good enough to ensure both stability and accuracy in approximating the singular term around the crack-tip as depicted in Fig. 3a)

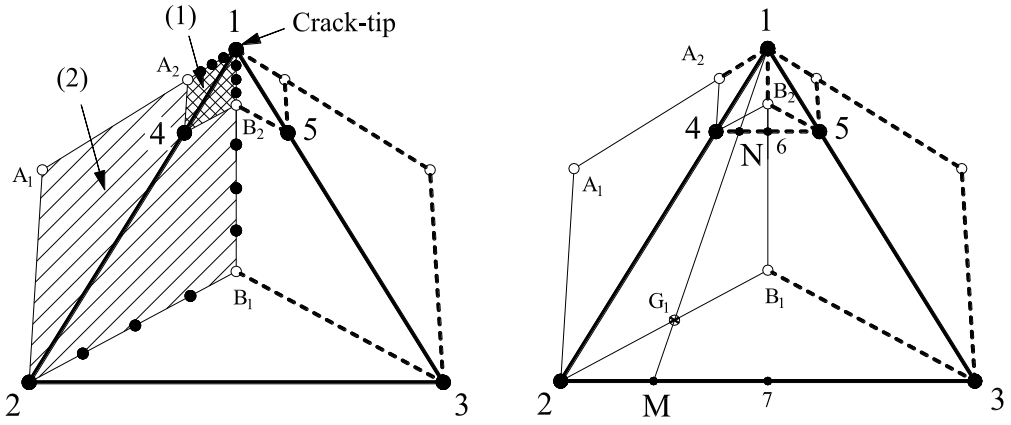

Figure 3.

a) Two layers of singular smoothing domains using three Gauss-point interpolation,

b) Additional node at arbitrary location in radial coordinate originated at the crack-tip

Along the arbitrary radial line 1-N-M, displacement is obtained using the Eq. (6) as

$$u = \Phi_1 u_1 + \Phi_2 u_N + \Phi_3 u_M \tag{10}$$

and

$$u_N = \left(1 - \frac{l_{N-4}}{l_{5-4}}\right)u_4 + \frac{l_{N-4}}{l_{5-4}}u_5,\quad u_M = \left(1 - \frac{l_{M-2}}{l_{3-2}}\right)u_2 + \frac{l_{M-2}}{l_{3-2}}u_3 \tag{11}$$

Similar triangle rule leads to $\frac{l_{N-4}}{l_{5-4}} = \frac{l_{M-2}}{l_{3-2}} = \alpha$. Substituting Eq. (11) into Eq. (10) yields

$$u = \Phi_1 u_1 + (1-\alpha)\Phi_3 u_2 + \alpha\Phi_3 u_3 + (1-\alpha)\Phi_2 u_4 + \alpha\Phi_2 u_5 \tag{12}$$

In matrix form: $u = \begin{bmatrix} N_1 & N_2 & N_3 & N_4 & N_5 \end{bmatrix} \begin{Bmatrix} d_1 & d_2 & d_3 & d_4 & d_5 \end{Bmatrix}^T = Nd$ (13)

where N is the matrix of shape functions of the singular element.

The smoothed strain–displacement matrix of each layer of singular smoothing domain is

$$\bar{B}_i^a = \begin{bmatrix} \bar{b}_{ix}^a & 0 \\ 0 & \bar{b}_{iy}^a \\ \bar{b}_{iy}^a & \bar{b}_{ix}^a \end{bmatrix} \text{ with } \bar{b}_{ix(y)}^a(x_k) = \frac{1}{A_k^{s,a}} \int_{\Gamma_k^{s,a}} N_i(x) n_{x(y)}^{k,a}(x) d\Gamma \tag{14}$$

where $A_k^{s,a}$, $\Gamma_k^{s,a}$ is the area and the boundary of the a-th layer of the singular SD $\Omega_k^{s,a}$, respectively, the shape functions $N_i(x)$ in Eq. (12) are adopted in this case, $n_{x(y)}^{k,a}$ is the unit normal vector of the boundary segment $\Gamma_k^{s,a}$

Similarly, we apply the Gauss integration along the segments of boundary $\Gamma_k^{s,a}$, then

$$\bar{b}_{ix(y)}^a = \frac{1}{A_k^{s,a}} \sum_{p=1}^{n_\Gamma^s} \left[\sum_{b=1}^{n_{Gauss}} w_{p,\mathrm{b}} n_{p,x(y)}^{k,a}(x) N_i\left(x_{p,b}^{Gauss}\right) \right] \tag{15}$$

where $n_{Gauss} = 3$ is the number of Gauss-points on each boundary segment Fig. 3a), $w_{p,\mathrm{b}}$ is the corresponding weight coefficient of the Gauss-points, $x_{p,b}^{Gauss}$ is the b-th Gauss-point of the pth boundary segment of $\Gamma_{k,p}^{s,a}$ and n_Γ^s is the number of boundary segments of $\sum_{p=1}^{n_\Gamma^s} \Gamma_{k,p}^{s,a} = \Gamma_k^{s,a}$

In this model, the Galerkin Weak Form is employed in a similar fashion to standard FEM-T3. However, the formulations of a stiffness matrix are associated with the smoothing domains, rather than individual members by

$$\bar{K} = \sum_{k=1}^{N_s} \bar{K}^k \tag{16}$$

and the nodal load vector $\tilde{f}$ is the same as that of the corresponding standard FEM-T3 as given below

$$\tilde{f}^e = \sum_{N_e} \int_{\Omega^e} N^T b^e d\Omega + \sum_{N_e} \int_{\Gamma_N^e} N^T t_N^e d\Gamma_N^e + \sum_{i=1}^{N_{node}} p_i \tag{17}$$

Adaptive Procedure

Recovery Based Strain Error Indicator

The global ZZ-type error indicator, η_Z , is the sum of the local ZZ-type error indicators from all individual elements in L2-norm, namely

$$\eta_Z = \left(\sum_{l=1}^{N_e} \eta_l^2 \right)^{1/2} \tag{18}$$

$$\eta_l = \left\| \bar{\sigma}_v - \bar{\sigma}_v^R \right\|_{L^2(\Omega_l)} = \left[\int_{\Omega_l} \left(\bar{\sigma}_v - \bar{\sigma}_v^R \right)^T \left(\bar{\sigma}_v - \bar{\sigma}_v^R \right) d\Omega \right]^{1/2} \tag{19}$$

where $\bar{\sigma}$ is the numerical solution of stress and is area-weight averaged using the stresses from the two layers of singular SDs that connected to the crack-tip by

$$\bar{\sigma}_i = \frac{A_k^{s,1} \bar{\sigma}_i^1 + A_k^{s,2} \bar{\sigma}_i^2}{A_k^s} \tag{20}$$

and $\bar{\sigma}^R$ is the recovery field of stress that is continuous over the entire domain and converges to an exact solution for a sufficiently fine mesh in ES-FEM-T3 obtained by

$$\bar{\sigma}^R = \sum_{i=1}^{n_n^e} N_i(x,y) \bar{\sigma}^R(i) \tag{21}$$

with $N_i(x,y)$ is the shape function at the i-th node (the same with standard FEM-T3), $\bar{\sigma}^R(i)$ is the vector containing the nodal stresses of an element (presenting the area-weight averaged stresses within smoothing singular ES-FEM-T3 domains see Fig. 4a,b,c)

$$\bar{\sigma}^R(\mathrm{i}) = \frac{1}{\mathrm{A}_i^{ns}} \sum_{k=1}^{n_s^i} \bar{\sigma}_k \, \mathrm{A}_k \tag{22}$$

in which n_s^i is the number of smoothing domains Ω_k^s around the i-th node, $\mathrm{A}_i^{ns} = \sum_{k=1}^{n_s^i} A_k$ is the total area of all the smoothing domains sharing the i-th node, and A_k is the area of the k-th smoothing domain sharing the i-th node

Note that: (1) the layer of singular SDs that close to the node will be considered case b) & c) Fig. 4. (2) for the standard ES-FEM-T3, the procedure simply take the case a) Fig. 4.

The formulation for a direct determination of the recovery-based error indicator is given by

$$\eta_l^2 = \| \bar{\sigma}_v - \bar{\sigma}_v^R \|_{L^2(\Omega_l)}^2 = \| \bar{\sigma}_v - \sum_{i=1}^{3} N_i(x,y) \bar{\sigma}_v^R(i) \|_{L^2(\Omega_l)}^2 = \sum_{q=1}^{3} \| \bar{\sigma}_{v,q} - \sum_{i=1}^{3} N_{i,q}(x,y) \bar{\sigma}_{v,q}^R(i) \|_{L^2(\Omega_{l,q})}^2 \tag{23}$$

where $\Omega_{l,q}$ is the q-th sub-smoothing domain (sub-SD) of the l-th element and $\bar{\sigma}_{v,q}^R(i)$ is the recovery nodal von Mises stress at the i-th node of the q-th sub-SD.

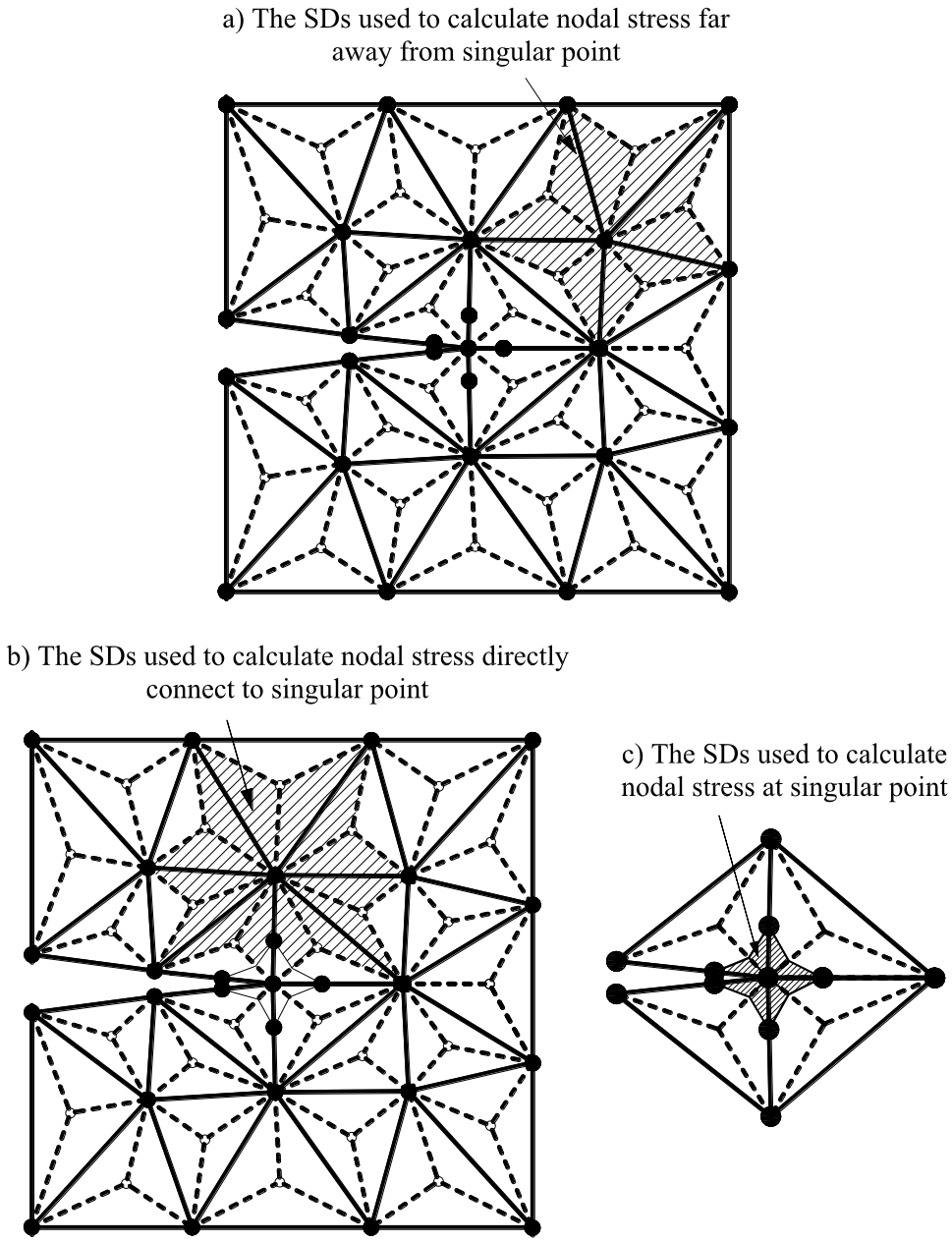

Figure 4. The smoothing domains used to calculate the nodal stress for nodes in the singular ES-FEM-T3

For each triangle element, there are three sub-SDs with constant smoothed stress and the recovery-based error indicator can be computed from their summation.
From the partition of unity property

$$\sum_{i=1}^{3} N_{i,q}(x,y) = 1 \tag{24}$$

$$\begin{aligned} \Rightarrow \eta_l^2 &= \sum_{q=1}^{3} \| \sum_{i=1}^{3} N_{i,q}(x,y)(\bar{\sigma}_{v,q}(i) - \bar{\sigma}_{v,q}^{R}(i)) \|_{L^2(\Omega_{l,q})}^2 \\ &= \sum_{q=1}^{3} \left[\sum_{i,j=1}^{3} \bar{r}_{l,\mathrm{q,i}} . \bar{r}_{l,\mathrm{q,j}} \int_{\Omega_{l,q}} N_{i,q}(x,y) N_{j,q}(x,y) d\Omega \right] \end{aligned} \tag{25}$$

where $\bar{r}_{l,\mathrm{q,i}} = \bar{\sigma}_{v,q}(i) - \bar{\sigma}^{R}_{v,q}(i)$ at i-th node

The shape function for each sub-SD satisfies

$$\int_{\Omega_{l,q}} N_{i,q}(x,y) N_{j,q}(x,y) d\Omega = \begin{cases} A_{l,q}/6 = A_l/18 & i = j \\ A_{l,q}/12 = A_l/36 & i \neq j \end{cases} \tag{26}$$

where $A_{l,q}$ is the area of the q-th sub-SD (covering one-third area) of the l-th element, and hence

$$\eta_l^2 = \sum_{q=1}^{3} (\bar{r}^2_{l,\mathrm{q},1} + \bar{r}^2_{l,\mathrm{q},2} + \bar{r}^2_{l,\mathrm{q},3} + \bar{r}_{l,\mathrm{q},1}.\bar{r}_{l,\mathrm{q},2} + \bar{r}_{l,\mathrm{q},1}.\bar{r}_{l,\mathrm{q},3} + \bar{r}_{l,\mathrm{q},2}.r_{l,\mathrm{q},3}).(A_l/18) \tag{27}$$

Refinement Strategy

Using the element refinement indicators, η_l, the well-known Dorfler criterion [12] defines the elements $\Omega^e \in \Omega_M$ for refinement, where the minimal set $\Omega_M \in \Omega$ satisfies

$$\theta \sum_{\Omega_l \in \Omega} \eta_l^2 \leq \sum_{\Omega_l \in \Omega_M} \eta_l^2 \text{ with } \theta \in (0,1) \tag{1}$$

A new mesh Ω' is generated from the refinement of at least the marked elements so-called M-Group $\Omega_M \in \Omega$ to reduce the total numerical error in the whole domain.

Newest Vertex Bisection Algorithm

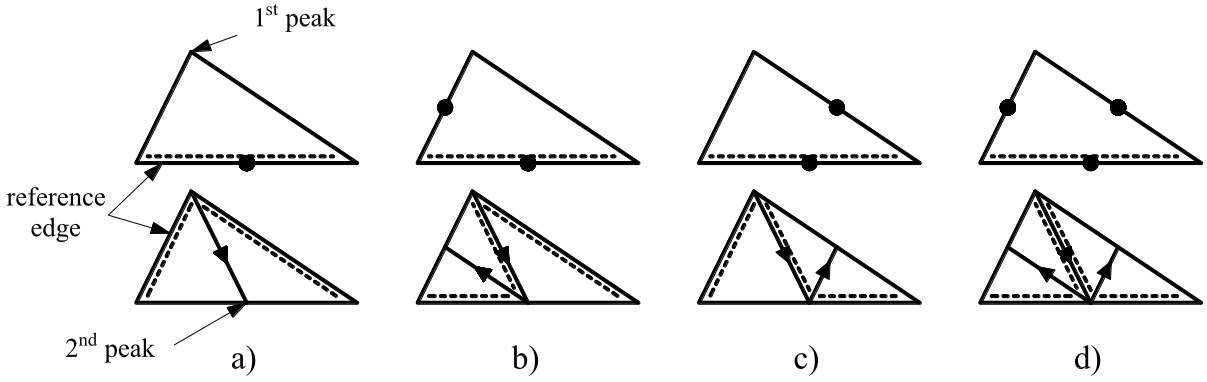

Figure 4. Four basic longest-edge mesh refinement patterns.

The Newest Vertex Bisection strategy [13], chooses to divide the parent element along the longest (reference) edge. This eliminates the capacity of producing triangles with smaller angles and the problem associated with hanging nodes [14]. Four typical types of partitioning a parent element into so-called child elements as in Fig. 4 are formed of lines connecting the newest (peak) vertex to the mid-point of the longest (reference) edge.

Refinement procedure:
(1) At least one reference edge (or dash-line) is marked for refinement.
(2) The newest vertex (midpoint) of reference edge becomes the peak for the next refinement step.
(3) The 2-nd refinement step is then implemented on the two other marked edges, if any from the newest peak.
* The same refinement procedure for each adaptive iteration.

Illustrative Examples

Two problems with difficulties under the presence of discontinuity and singularity stress field are tested. The ES-FEM-T3 model were applied and encoded within a MATLAB environment using built-in function and vector language. A layer of five-node singular elements is employed in crack problems to validate the accuracy and robustness of the proposed analysis framework.

Example 1: Prandtl's Punch

A plane-strain Prandtl's punch problem with flexible foundation is drawn in Fig. 5. A total of uniformly distributed loads of 10 represents for the footing length of 2. The material properties employed were: $E = 10^4$, $v = 0.25$ and $t = 1$. Due to the symmetry of both geometry and loading configurations, only half of the structure is modeled. The characteristic discrete structural model in Fig. 5b) contains 256 simple triangle elements.

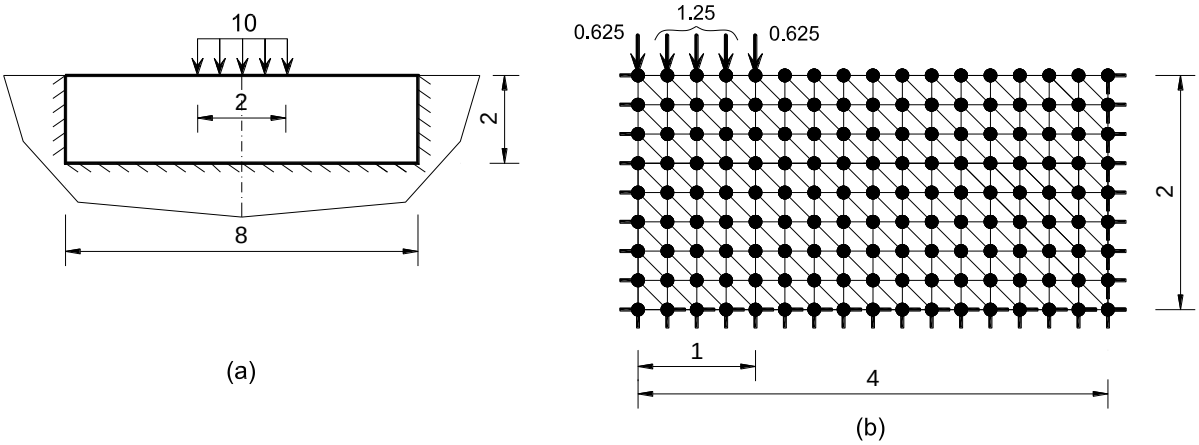

Figure 5. Example 1: Prandtl's punch (a) geometry and loading, (b) characteristic ES-FEM-T3 model, where thick solid lines denote nodal restrained directions.

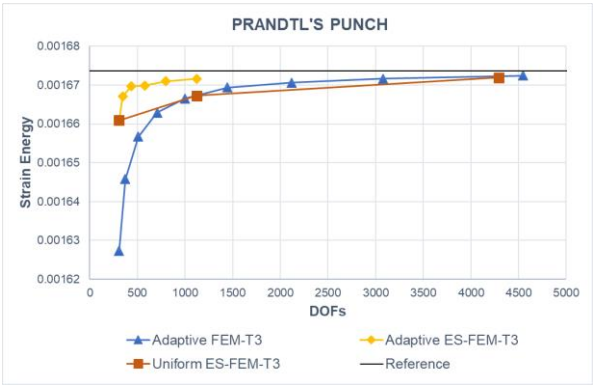

Figure 6. Example 1: Convergence of strain energy results from various analysis methods.

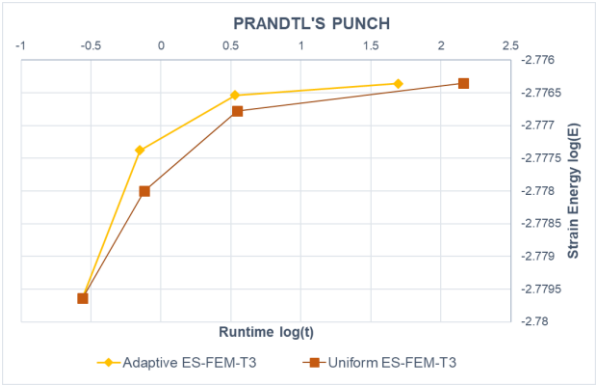

Figure 7. Example 1: Convergence rate of runtime versus strain energy between adaptive ES-FEM-T3 and uniform ES-FEM-T3.

The proposed automatic adaptive ES-FEM-T3 analysis approach was successfully processed to obtain elastic strain energy response solutions. The analysis results computed are plotted with their associated DOFs in Fig. 6, where those of some other standard FEMs, namely FEM-T3 with mesh adaptive scheme and ES-FEM-T3 with uniform mesh refinement. It is clear that all methods yield the solutions converged to the reference value at the sufficient fine

numbers of discrete elements. In addition, the proposed automatic adaptive ES-FEM-T3 approach provided the fast-converged strain energy solutions as compared to ES-FEM-T3 with uniform mesh refinement. The computing times as required for successfully converging the results by automatic mesh adaptive recovery-based strain algorithm, as displayed in Fig. 7, were less than those from standard uniform mesh refining technique.

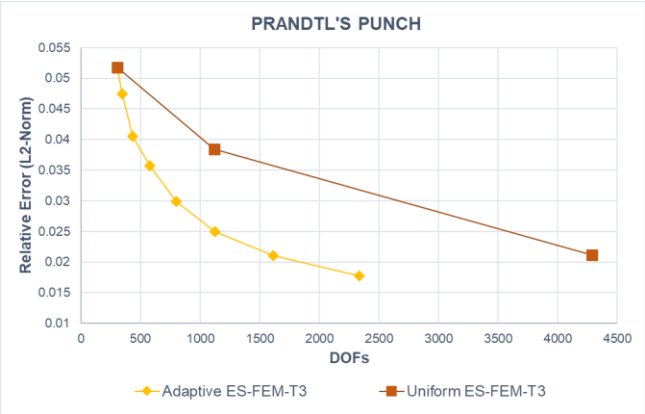

Figure 8. Example 1: Convergence of relative error results from adaptive ES-FEM-T3 and uniform ES-FEM-T3.

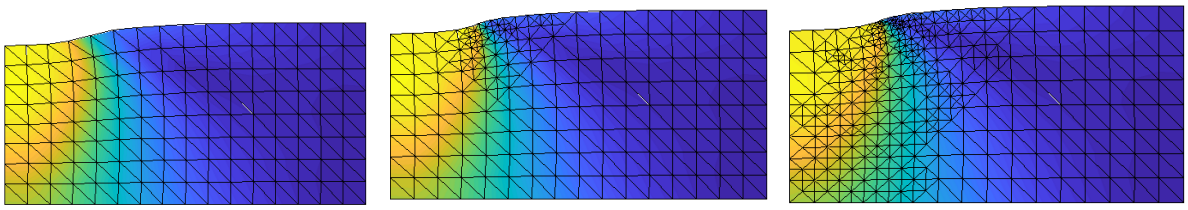

(a) 256 ele. (error 5.17%) - (b) 379 ele. (error 4.18%) - (c) 758 ele. (error 3.14%)

Figure 9. Example 1: Automatic adaptive meshes with the corresponding contour line of von Mises stress distributions.

The present adaptive mesh implementation dramatically reduces the recovery-based relative error compared to a slow reduction using the normal uniform refinement strategy. The values from adaptive ES-FEM-T3 fast approach the zero value, while those from uniform ES-FEM-T3 is still at a very high value in Fig. 8. The von Mises stress results corresponding to automatically adaptive meshes are depicted in Fig. 9. It illustrates the mesh refinements localizing over strong discontinuity areas of applied load.

Example 2: Double-Edge Notched Specimen

The second example considers a plane strain double-edge notched specimen as depicted in Fig. 10 subjected to the total uniform lateral load of 1.44 on both end edges. The material properties of E = 70, v = 0.3 and t = 1 were adopted. Because of symmetry in both x-axis and y-axis, only a quarter of the specimen without undue loss of accuracy was analyzed. The initial characteristic ES-FEM-T3 with 150 elements is displayed in Fig. 10b)

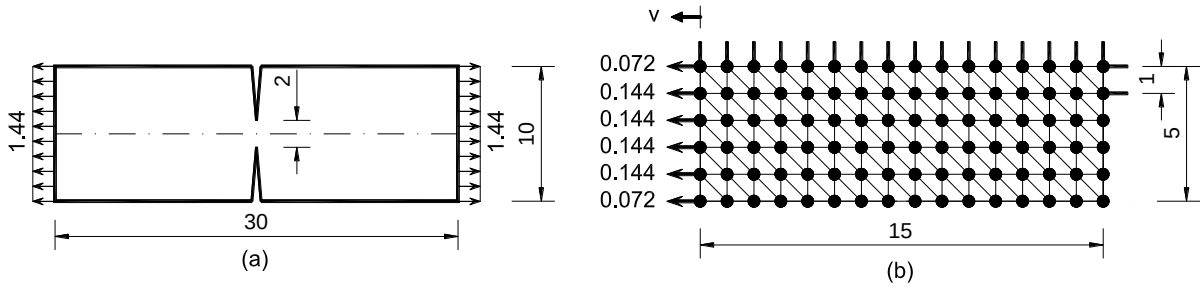

Figure 10. Example 2: Double-edge notched specimen (a) Initial mesh and loading (b) ES-FEM-T3 model, where thick solid lines denote nodal restrained directions.

The ES-FEM-T3 incorporated the automatic adaptive scheme adopting recovery-based strain error functions. The lateral displacements v and strain energy responses (displayed in Figs.11 and 12, respectively) were successfully computed for various mesh refinements, and compared with those found from other standard FEM-T3 with the similar adaptive mesh algorithm.

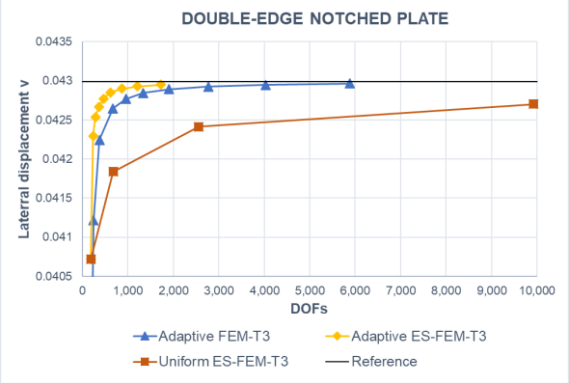

Figure 11. Example 2: Convergence of lateral displacement results for various automatic adaptive mesh algorithms.

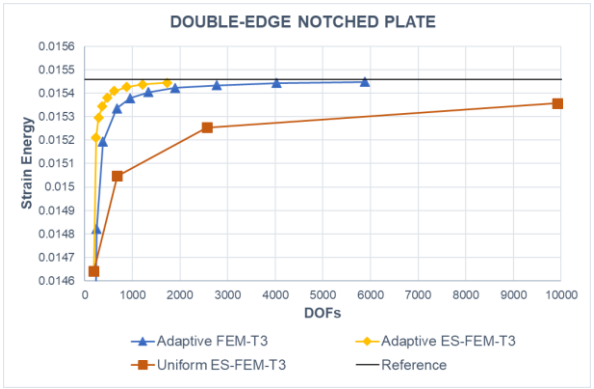

Figure 12. Example 2: Convergence of strain energy results for various automatic adaptive mesh algorithms

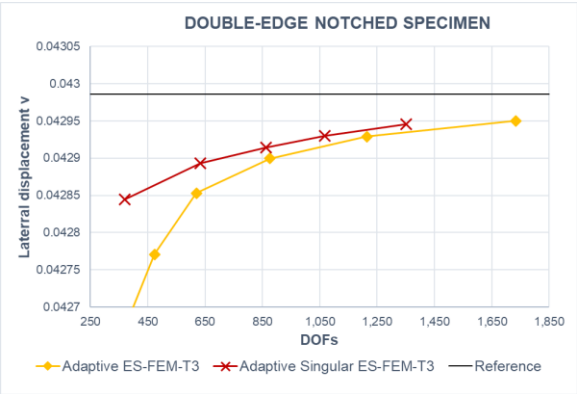

Figure 13. Example 2: Convergence of lateral displacement results from adaptive ES-FEM-T3 and adaptive singular ES-FEM-T3

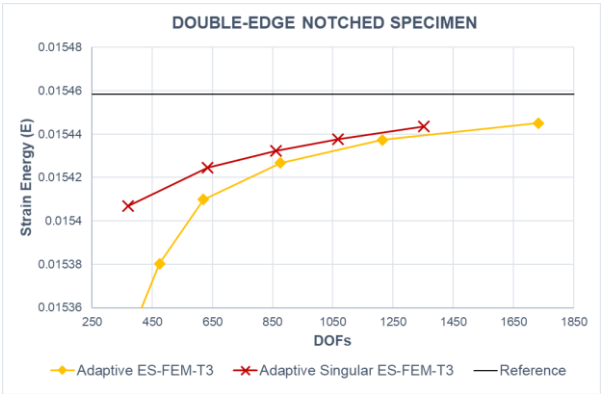

Figure 14. Example 2: Convergence of strain energy results from adaptive ES-FEM-T3 and adaptive singular ES-FEM-T3

After adopting a layer of singular five-node elements around the crack-tip, the results obtained from the adaptive singular ES-FEM-T3 converge with a more reasonable computing efforts (DOFs) in terms of both the lateral displacements v and strain energy solutions (as depicted in Figs. 13 & 14, respectively). In addition, both models incorporated the same automatic adaptive scheme adopting recovery-based strain error functions converge to the reference values.

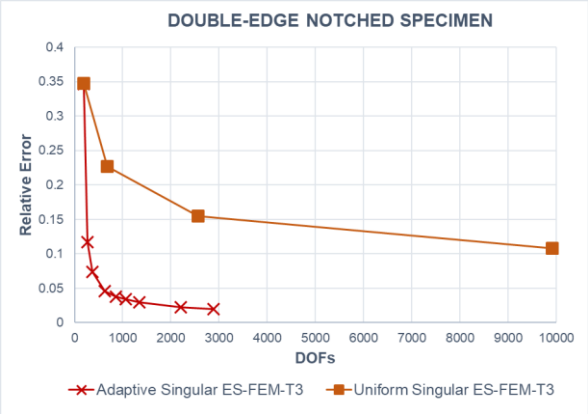

Figure 15. Example 2: Convergence of relative error results from adaptive singular ES-FEM-T3 and uniform singular ES-FEM-T3

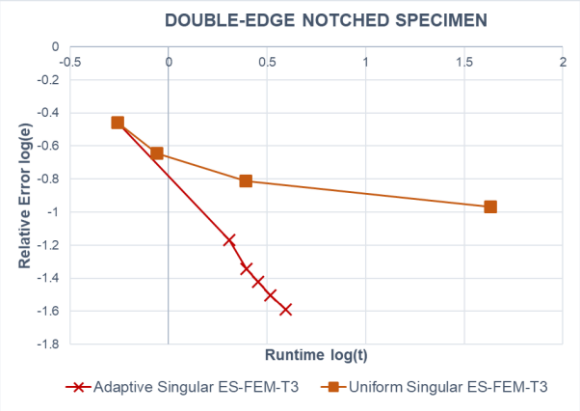

Figure 16. Example 2: Convergence rate of runtime versus relative error between adaptive singular ES-FEM-T3 and uniform singular ES-FEM-T3.

Within the framework of singular ES-FEM-T3, the present adaptive mesh implementation dramatically reduces relative error with less computing efforts (i.e. both DOFs and runtime as in Figs. 15 & 16) compared to standard model adopting uniform refinement strategy. Relative errors from adaptive singular ES-FEM-T3 navigates to the zero value, while those obtained from uniform singular ES-FEM-T3 are still at a very high value (i.e. less than 5% can be obtained with about 500 DOFs as shown in Fig. 15. It is clear that the convergence rate in a log scale equals 1:1 for adaptive singular ES-FEM-T3 and around 1:3 for uniform singular ES-FEM-T3 from Fig. 16.

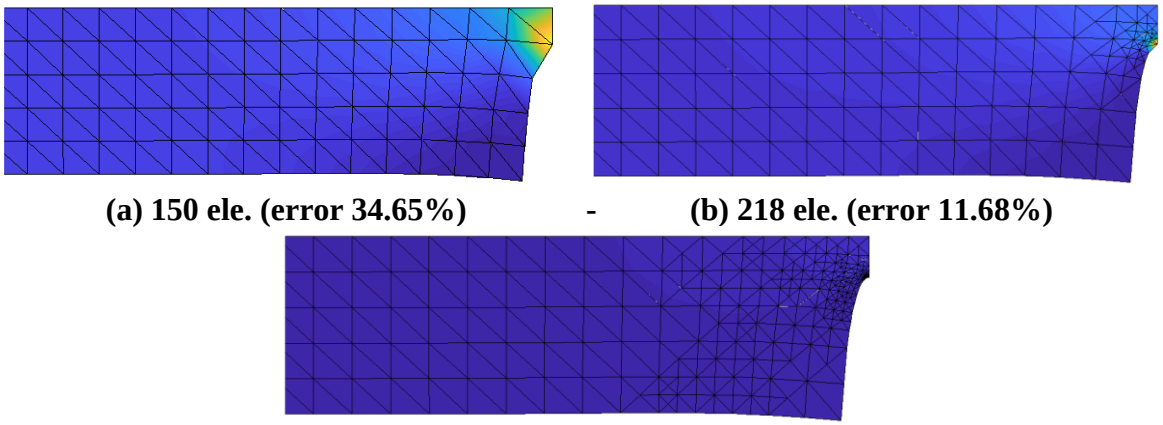

(a) 150 ele. (error 34.65%) - **(b) 218 ele. (error 11.68%)**

(c) 568 ele. (error 4.57%)

Figure 17. Example 2: Automatic adaptive meshes with the corresponding contour line of von Mises stress distributions.

The mesh discretized patterns in Fig. 17 as expected progressively refined over the concentrated stress singularity and discontinuity areas.

Conclusions

The novel ES-FEM-T3 and singular ES-FEM-T3 approaches employed automatic AMR algorithm to efficiently and accurately provide the response solution of elastic structures. The automatic AMR adopted the newest vertex bisection algorithm and recovery-based error function in L2-norm. A number of numerical examples (including both benchmarks and practical in-plane structures) were successfully solved using the proposed analysis scheme. Three of which are given in this study. These illustrate robustness of the proposed analysis method, in which the adaptive singular ES-FEM-T3 approach provided the superconvergence of elastic response solutions as compared to the other models for crack problems and the adaptive ES-FEM-T3 approach for general discontinuity problems (i.e. discontinuity applied load). The computed results agreed well with all reference values, and thus evidenced the computational advantages in yielding the close-to-exact solutions for modest computing resources.

A nontrivial extension of the proposed analysis framework is to apply into contact or nonlinear fracture problems (i.e. using cohesive fracture model). A new error estimation (i.e. the simple splitting the normal and singular parts of stress field, similar to [15]) that is suitable for the five-node singular elements is also our interest.

Acknowledgement

The financial support from Chulalongkorn University through Applied Mechanics and Structure Research Unit is acknowledged. The first author would also like to thank the ASEAN Full-Scholarship.

References

1. Liu, G., K. Dai, and T.T. Nguyen, *A smoothed finite element method for mechanics problems.* Computational Mechanics, 2007. **39**(6): p. 859-877.
2. Chen, J.S., et al., *A stabilized conforming nodal integration for Galerkin mesh-free methods.* International journal for numerical methods in engineering, 2001. **50**(2): p. 435-466.
3. Nourbakhshnia, N. and G. Liu, *A quasi-static crack growth simulation based on the singular ES-FEM.* International Journal for Numerical Methods in Engineering, 2011. **88**(5): p. 473-492.
4. Nguyen-Xuan, H., et al., *An adaptive singular ES-FEM for mechanics problems with singular field of arbitrary order.* Computer Methods in Applied Mechanics and Engineering, 2013. **253**: p. 252-273.
5. Nguyen-Thoi, T., et al., *Adaptive analysis using the node-based smoothed finite element method (NS-FEM).* International Journal for Numerical Methods in Biomedical Engineering, 2011. **27**(2): p. 198-218.
6. Tangaramvong, S., F. Tin-Loi, and C. Song, *A direct complementarity approach for the elastoplastic analysis of plane stress and plane strain structures.* International Journal for Numerical Methods in Engineering, 2012. **90**(7): p. 838-866.
7. Vicente da Silva, M. and A. Antao, *A non-linear programming method approach for upper bound limit analysis.* International Journal for Numerical Methods in Engineering, 2007. **72**(10): p. 1192-1218.
8. Szabó, B., B.A. Szabo, and I. Babuška, *Finite element analysis*. 1991: John Wiley & Sons.
9. Williams, M., *Stress singularities resulting from various boundary conditions in angular corners of plates in extension.* Journal of applied mechanics, 1952. **19**(4): p. 526-528.
10. Seweryn, A. and K. Molski, *Elastic stress singularities and corresponding generalized stress intensity factors for angular corners under various boundary conditions.* Engineering Fracture Mechanics, 1996. **55**(4): p. 529-556.
11. Zienkiewicz, O.C., et al., *The finite element method: solid mechanics*. Vol. 2. 2000: Butterworth-heinemann.
12. Dörfler, W., *A convergent adaptive algorithm for Poisson's equation.* SIAM Journal on Numerical Analysis, 1996. **33**(3): p. 1106-1124.
13. Rivara, M.C., *Algorithms for refining triangular grids suitable for adaptive and multigrid techniques.* International journal for numerical methods in Engineering, 1984. **20**(4): p. 745-756.
14. CHEN, L. *Short implementation of bisection in MATLAB*. in *Recent Advances In Computational Sciences: Selected Papers from the International Workshop on Computational Sciences and Its Education*. 2008. World Scientific.
15. Ródenas, J.J., et al., *A recovery-type error estimator for the extended finite element method based on singular+ smooth stress field splitting.* International Journal for Numerical Methods in Engineering, 2008. **76**(4): p. 545-571.